Journal of Materials Chemistry A

PAPER

View Article Online
View Journal | View Issue

Cite this: J. Mater. Chem. A, 2014, 2, 11913

Enhanced thermoelectric performance of a new half-Heusler derivative $Zr_9Ni_7Sn_8$ bulk nanocomposite: enhanced electrical conductivity and low thermal conductivity†

D. K. Misra,*[a] A. Bhardwaj[a] and Sanjay Singh[b]

Received 21st March 2014
Accepted 24th April 2014

DOI: 10.1039/c4ta01380h

www.rsc.org/MaterialsA

Varying the valence electron concentration per unit cell (VEC) in a half-Heusler (HH) material gives a large number of structures and substructures that can be exploited to improve the thermoelectric performance. Herein, we studied $Zr_9Ni_7Sn_8$ with VEC = 17.25, which is smaller than 18 for normal ZrNiSn half-Heusler, to explore the structural modifications for improvement of thermoelectric performance. The structural analysis employing XRD, SEM and TEM confirms the resulting material to be a composite of HH and Ni_3Sn_4-type phases. Rietveld analysis estimates the volume fraction of HH to be 75.6 ± 1.2% and 24.6 ± 0.8% for Ni_3Sn_4 phase. Interestingly, the present composite results in a substantial increase in electrical conductivity (σ) by ~75% and a drastic reduction in thermal conductivity (κ) by ~56%, leading to a thermoelectric figure of merit (ZT) of 0.38 at 773 K, which is ~85% higher than in normal HH ZrNiSn. Further, the nanostructuring of the composite, achieved by mechanical milling, derives a significantly reduced κ (*i.e.* from 4.56 W m^{-1} K^{-1} to 3.36 W m^{-1} K^{-1}, at 323 K), yielding a ZT of 0.90 at 773 K, which is >300% enhancement over the normal HH. The experimental results have been compared with the Bergman and Fel model for calculating effective thermoelectric parameters in composites.

1. Introduction

Thermoelectricity, being the simplest technology for the conversion of thermal energy to electrical energy has attracted renewed attention for application in power generation. In the past decade, most efforts have concentrated on thermoelectric research dealing with designing new materials or optimizing existing materials to increase their conversion efficiency. The greatest challenge in this direction lies in the optimization of three competing physical material property parameters perceived in the expression of the dimensionless thermoelectric figure of merit,[1] $ZT = (\alpha^2\sigma T)/\kappa$, where α is the Seebeck coefficient, σ is the electrical conductivity, T the absolute temperature and κ is the thermal conductivity. The modification of any of these physical parameters α, σ and κ often adversely affects the other due to their interdependence and hence limits the increase in the overall ZT.

The best possible strategy for increasing ZT is to decouple the thermoelectric parameters; α, σ and κ by doping, solid solution alloying and nanostructuring approaches. These concepts have been demonstrated theoretically and experimentally in several systems, such as, Bi_2Te_3,[2–6] $AgPb_mSbTe_{2+m}$ (LAST),[7] TeAgGeSb,[8] PbTe,[9] SiGe[10] and Zintl phase compounds.[11–15] Despite their high ZT, these materials are not viable for economic and large scale commercial applications because their constituents are expensive and toxic.

Among several thermoelectric materials, HH compounds have been identified not only as a promising class of thermoelectric materials[16–19] but also they possesses various properties such as being magnetic,[20,21] topological insulators,[22,23] having shape memory,[24,25] thermoelectric[16–19] *etc.* with their varying VEC. They are composed of cheap, non-toxic elements and are easy to synthesize on a large scale. Interestingly, these materials exhibit reasonably high σ due to narrow band gaps, and large α due to high slopes of density of state near the Fermi level. However, despite these excellent electronic properties, they exhibit low ZTs due to their relatively high κ.

In the past decades, several approaches such as controlled doping, solid solution alloying and nanostructuring in HH compounds have been adopted to disrupt the heat carrying phonons in order to achieve significant reduction in their κ. Recently, a chemical disorder of full-Heusler (FH) at the atomic scale in a half-Heusler matrix, the so called Atomic-Scale Structural Engineering of Thermoelectrics (ASSET) approach, has been employed in both p-type MCoSb (where M = Ti, Zr, Hf)

[a]CSIR-Network of Institutes for Solar Energy, Materials Physics & Engineering Division, CSIR-National Physical Laboratory, Dr K. S. Krishnan Marg, New Delhi-110012, India. E-mail: misradk@nplindia.org; dakkmisra@gmail.com

[b]Surface Physics Division, Saha Institute of Nuclear Physics, Sector-I, block-'AF', Bidhannagar, Kolkata-700064, India

† Electronic supplementary information (ESI) available. See DOI: 10.1039/c4ta01380h

and in n-type MNiSn HH to reduce κ further. Moreover, it has also been reported that κ in a half-Heusler material can be significantly reduced by making a super cell of HH with increased unit cell based on varying the VEC, which has been achieved in $Ru_9Zn_7Sb_8$. It has been claimed that a significant reduction in κ, about one quarter of that of most normal HH materials, is obtained due to the superstructure of HH in $Ru_9Zn_7Sn_8$.[26] It is also suggested that the compound $Ru_9Zn_7Sb_8$ and its analogues $M_9Zn_7Sb_8$ (M = Fe, Co, Rh) could serve as a new structure type for exploring new thermoelectric materials. Despite this, a further reduction in their κ could make these materials more efficient for commercial applications.

The concept of nanostructuring and nanocomposites has been observed to improve the efficiency of thermoelectric devices for power generation due to their capability of decoupling the competing physical parameters; σ, α and κ, leading to an enhancement in *ZT*. The nanocomposite materials could be either single-phase nanomaterials or nanoinclusions embedded in a host bulk matrix, the latter being the most common nanocomposite approach. The micron-scale and nanometer-scale inclusions in the nanocomposite facilitate some of the limitations that otherwise arise from interrelated α, σ and κ in their counterpart bulk materials.[27–29] The nanocomposite thermoelectric materials exhibit several requisite features for the optimization of a high *ZT*, such as, (1) numerous grain boundaries which can scatter phonons effectively for the reduction in κ,[30,31] (2) mechanisms of energy dependent scattering of electrons at interfaces between the matrix and nanoinclusions *i.e.*, an electron filtering effect[32,33] for improvement of the power factor ($\alpha^2\sigma$), (3) an electron injecting phenomenon induced by the nanoinclusions, (4) a quantum confinement regime which alters the electronic structure and phonon dispersion relationship,[7,29,34] (5) morphological tailoring of nanocomposite thermoelectric materials due to dimensional reduction, grain refinement and size reduction of a second phase.[35–39]

However, despite of all these interesting features, inherent limitations of the composite materials can also be noted in light of the established theory of effective medium approximation (EMA) by Bergman and Fel.[40,41] This study demonstrates that the σ and κ of a composite can not be improved for high *ZT*, in comparison with that of either the best or worst thermoelectric parameter of the separate components of the composite, if the contribution from the phase interface/boundary is of little worth.[40,41] The thermoelectric properties calculated by them for the binary composite indicated that the *ZT* of the composite could never exceed the highest *ZT* of each separate component phase, although enhancement in the power factor could be achieved. The proof-of-principle of the EMA theory was demonstrated experimentally by Heremans *et al.*[42] in a composite of high thermopower Bi matrix and high electrically conducting inclusions of Ag. However, recently the nanocomposites based on PbTe,[9] $CoSb_3$,[43–45] Bi_2Te_3,[2–6] Mg_2Si,[11] and HH'[46–49] as the matrix phase deliver simultaneous improvement in the power factor and reduction in κ leading to an increased *ZT*. It may be emphasized that the enhancement in *ZT* in most of these nanocomposites resulted almost entirely from a drastic reduction of the lattice thermal conductivity (κ_l), due to increased phonon scattering at several interfaces and grain boundaries. In such nanocomposites, the dispersed nanoparticles are designed to scatter the phonons more effectively than electrons because the mean free path of phonons is comparable to the grain size while the micro-particle matrix forms a connected network for electron transport. This leads to partial decoupling of the thermal and electronic transport. Thus, it is expected that the nanocomposite containing more fine particles may have low σ and low κ. Furthermore, α usually does not change significantly by changing the grain size and hence the *ZT* value could be tuned by reducing κ by optimizing the volume percentage of fine inclusions.

In the present work, a new undoped non-stoichiometric HH based composition of $Zr_9Ni_7Sn_8$ having a VEC of 17.25 per formula unit, which is smaller than 18 for normal ZrNiSn HH, has been synthesized in order to obtain either the superstructure of HH, if it occurs similar to the report of $Ru_9Zn_7Sb_8$, or a composite phase material if phase segregation occurs. We noticed that despite the formation of a single phase supercell of HH phase, two separate phases of HH (space group; $F\bar{4}3m$; cubic) and Ni_3Sn_4 (space group; $C2/m(12)$; monoclinic) were stabilized resulting in a HH composite phase. In order to ascertain the phases obtained, the composition $Zr_9Ni_7Sn_8$ has been optimized by several synthesis routes such as solid state reaction, ball-milling and arc-melting. The resulting composite has high reproducibility which has been verified by the various synthetic approaches. We observed that this large mismatch in VEC number, compared with that of $Ru_9Zn_7Sb_8$ (VEC = 15.75 per formula unit), does not allow this composition to be stabilized electronically as a supercell of HH; rather it causes phase separation of the system, resulting in a composite of HH ZrNiSn and Ni_3Sn_4 phase. Interestingly, despite the metallic nature of Ni_3Sn_4 (with larger κ at room temperature than that of the HH phase), a drastic reduction in thermal conductivity (~56%) was observed, which might originate from the dampening of lattice thermal conductivity ($\kappa_{lattice}$) by metallic Ni_3Sn_4 inclusion. These inclusions of Ni_3Sn_4 do not act as an accelerated path for thermal transport, and thereby result in a decrease in thermal conductivity. Moreover, the interfaces of HH and Ni_3Sn_4 phase disrupt the phonon transport which leads to medium-to-long wavelength phonon scattering, thus resulting in reduction of $\kappa_{lattice}$. The nanostructuring (employed by mechanical ball milling) further induces increased density of such hetero-interfaces of HH/Ni_3Sn_4 which yields a further reduction in thermal conductivity, leading to a *ZT* of 0.90 at 773 K. Such an *in situ* bulk nanocomposite (BNC) in $Zr_9Ni_7Sn_8$ with VEC = 17.25 per formula unit which is smaller than 18 for normal HH ZrNiSn, resulted in partitioning of a precursor phase into primarily two thermodynamically stable phases, providing additional control of the optimization of thermoelectric parameters for enhancement of *ZT*. The present strategy of fabricating an *in situ* bulk nanocomposite by decreasing the VEC below that of the HH leading to a high *ZT via* drastic reduction in thermal conductivity may be extended to explore several compositions in the XYZ (X = Ti, Zr, Hf, Y = Ni, Co, Z = Sn, Sb) family of half-Heusler materials.

2. Experimental details

The stoichiometric compositions of ZrNiSn, $Zr_9Ni_7Sn_8$ and Ni_3Sn_4 phase were prepared by melting zirconium (Zr; 99.99%, Alfa Aesar), nickel (Ni; 99.99%, Alfa Aesar), and tin (Sn; 99.99%, Alfa Aesar) powders using an arc-melting process. All the elemental powders for each stoichiometry were mixed together and cold pressed into cylindrical pellets for further use in Arc melts. The congealed melts were re-melted several times in the arc melter after turning them over to ensure homogeneity. The melted ingot was then annealed at 1173 K for one week under vacuum in a quartz tube. All the final ingots were pulverized into fine powders and consolidated by employing a spark plasma sintering (SPS) technique at a temperature of 1073 K and pressure of 50 MPa for a holding time of 10 minutes using graphite dies with a 12.7 mm central cylindrical opening to form dense pellets. In the present study, ZrNiSn is designated as HH and $Zr_9Ni_7Sn_8$ is termed as bulk composite (BC). A portion of the annealed sample of $Zr_9Ni_7Sn_8$ was further milled for 30 hours to reduce the grain size. The mechanically milled nano-powder of $Zr_9Ni_7Sn_8$ was then consolidated under the same conditions using SPS to obtain a 12.7 mm diameter sample of nanostructured composite, which is designated as bulk nano-composite (BNC). The samples were characterized by powder X-ray diffraction (Rigaku Mini Flex II), Scanning Electron Microscopy (SEM) and Transmission Electron Microscopy (TEM; Technai G^2 T^{30}; W-Twin operating at 300 KV) to study their phases, homogeneity, average grain sizes, and the grain-size distributions of the minor phases.

The electrical conductivity and Seebeck coefficient were measured simultaneously by employing the commercial equipment (ULVAC, ZEM-3) in the temperature range 300 to 773 K on samples of polished bars of about $3 \times 2 \times 10$ mm. The electrical conductivity was measured in four probe geometry. The thermal diffusivity was measured with disks of 12.7 mm in diameter and 2 mm in thickness in the same temperature range using a laser flash system (Lineseis, LFA 1000). The disc specimen used for thermal diffusivity was sprayed with a layer of graphite in order to minimize errors due to emissivity. Specific heat was determined by a Differential Scanning Calorimeter (DSC 822^e Mettler Toledo). The thermal conductivity was calculated as $\kappa = \alpha C_p \rho$ where α, C_p and ρ are the thermal diffusivity, specific heat capacity and density, respectively.

Reproducibility of the thermoelectric properties was realized within 3% under the same experimental conditions. The density of the sintered samples was measured using an Archimedes' kit and was observed to be >98% of the theoretical density.

3. Results and discussion

3.1 Structural characterization

The XRD patterns of SPSed normal half-Heusler-ZrNiSn (HH), bulk composite-$Zr_9Ni_7Sn_8$ (BC) and bulk nanocomposite-$Zr_9Ni_7Sn_8$ (BNC) are presented in Fig. 1. All the peaks in the XRD patterns corresponding to the ZrNiSn sample (Fig. 1a), could be well indexed to the cubic crystal system (space group $F\bar{4}3m$).

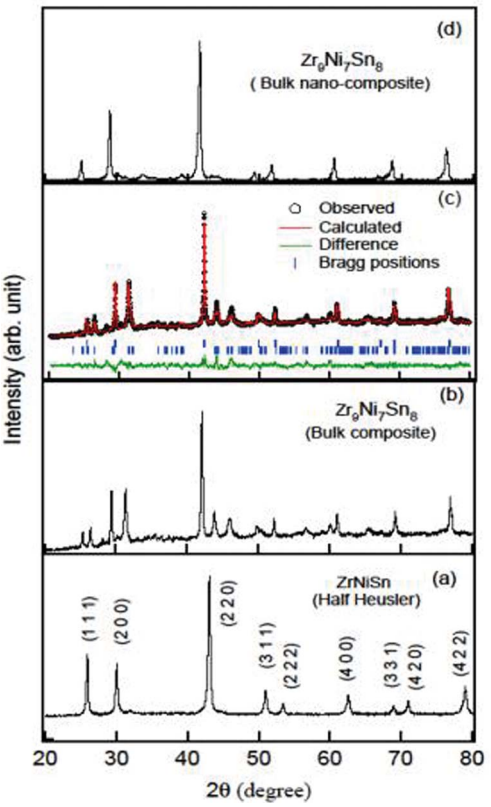

Fig. 1 X-ray diffraction patterns of (a) ZrNiSn HH, (b) BC $Zr_9Ni_7Sn_8$, HH derivative, (c) Reitveld refinement of $Zr_9Ni_7Sn_8$ showing a composite which is well indexed to the HH and Ni_3Sn_4 phases, blue ticks are Bragg positions with the upper blue ticks corresponding to the HH and the lower blue ticks are for Ni_3Sn_4 phase and (d) bulk nanocomposite (BNC) $Zr_9Ni_7Sn_8$.

Fig. 1b shows the XRD pattern which indicates the co-existence of two separate phases, namely HH as the major phase and monoclinic Ni_3Sn_4 (space group; $C2/m(12)$) as the minor phase. The Reitveld refinement (Fig. 1c) of BC $Zr_9Ni_7Sn_8$ was performed to calculate the lattice parameter in the composites, which is shown in Table 1. Thus, despite formation of a supercell, as reported in $Ru_9Zn_7Sb_8$,[26] $Zr_9Ni_7Sn_8$ forms a composite material consisting of a slightly larger unit cell of HH in comparison to the normal ZrNiSn HH (Fig. 1b). This expansion of the unit cell of HH becomes more prominent in the BNC $Zr_9Ni_7Sn_8$ sample (Fig. 1d). Moreover, a subtle peak broadening in HH peaks (Fig. 1d) was also noted indicating the reduced size of the HH grains in the BNC sample prepared by the nanostructuring route.

Table 1 Lattice parameters of ZrNiSn normal HH, $Zr_9Ni_7Sn_8$ bulk composite (BC) and $Zr_9Ni_7Sn_8$ bulk nanocomposite (BNC) samples obtained from the Reitveld analysis

Lattice parameter	HH-ZrNiSn	BC-$Zr_9Ni_7Sn_8$	BNC-$Zr_9Ni_7Sn_8$
'a' value	6.04 Å	6.10 Å	6.18 Å

In order to further identify the phases and microstructural details, SEM and TEM of BC and BNC samples were performed. The SEM morphology of BC sample is shown in Fig. 2a, and clearly reveals a two phase contrast, indicating a composite composed of two phases. The EDAX analysis of this sample in Fig. 2b and c, clearly reveals the dark grey contrast (marked as doted curves) to be the HH phase while the light grey contrast (marked as square boxes) is the Ni_3Sn_4 phase. The EDAX result (Fig. 2c) obtained from the light grey contrast grain shows a composition of $Ni_{3.01}Sn_{4.1}Zr_{0.3}$ indicating additional Zr which might have originated from the grain boundary of Ni_3Sn_4 obtained during phase separation.

In order to confirm the phases present in the BC $Zr_9Ni_7Sn_8$ sample, TEM was carried out. A two phase contrast in the bright field TEM image (Fig. 2d) is observed which is consistent with the phases shown in the SEM image (Fig. 2a). To clarify the phase contrast, a high magnification TEM image is recorded, which is shown in Fig. 2e. The selected area electron diffraction (SAED) pattern taken from the light contrast portion (the dotted area) in Fig. 2e, shown in the inset, reveals the dotted marked area to be the HH phase. The EDAX analysis from a dark contrast region (in Fig. 2e) again confirms it to be a Ni_3Sn_4-type phase (not shown here). The formation of Ni_3Sn_4-type phase within the HH matrix in $Zr_9Ni_7Sn_8$ resulting from arc melting could be attributed to occur due to phase separation during cooling. A single solid solution of all the elements at high temperature decomposes into thermodynamically stable phases of HH and Ni_3Sn_4-type phase at lower temperature. TEM characterization of the BNC sample, synthesized by nanostructuring route, was also performed. Fig. 3a shows bright field TEM images obtained of the BNC sample clearly showing a co-existence of two phase contrast together with highly densely packed grains of smaller sizes. The HRTEM image shown in Fig. 3b confirms that the dark precipitates correspond to (−5, 1, 1) planes of Ni_3Sn_4 phases, while the SAED pattern in Fig. 3c, obtained from the grey contrast, corresponds to the [−1 1 1] zone axis of HH. The microstructure (Fig. 3a) of the BNC sample reveals a high density of grains with smaller sizes as compared to the normal BC. The size of HH grains of the BNC sample ranges from 45 to 170 nm, which is much smaller than the grains ranging from 0.3 to 2 μm for the BC sample. Thus, the present microstructural analysis reveals that the BNC sample consists of different scaled hierarchical architectures starting from nanoscale Ni_3Sn_4 (5–25 nm) to mesoscale HH grain boundaries (45–170 nm).

3.2 Thermoelectric properties

In order to understand the impact of such an *in situ* fabricated composite with multiple length scale dimensions on the thermoelectric properties, both the $Zr_9Ni_7Sn_8$ BC and BNC samples were subjected to thermal and electronic transport measurements. The electronic and thermal transport properties of BC and BNC samples have been studied and compared with the normal HH. Fig. 4 shows the temperature dependence of various electrical and thermal parameters which contributed towards *ZT*. The electrical conductivity of all the samples increases monotonically with increasing temperature, displaying a characteristic feature of semiconducting materials. The

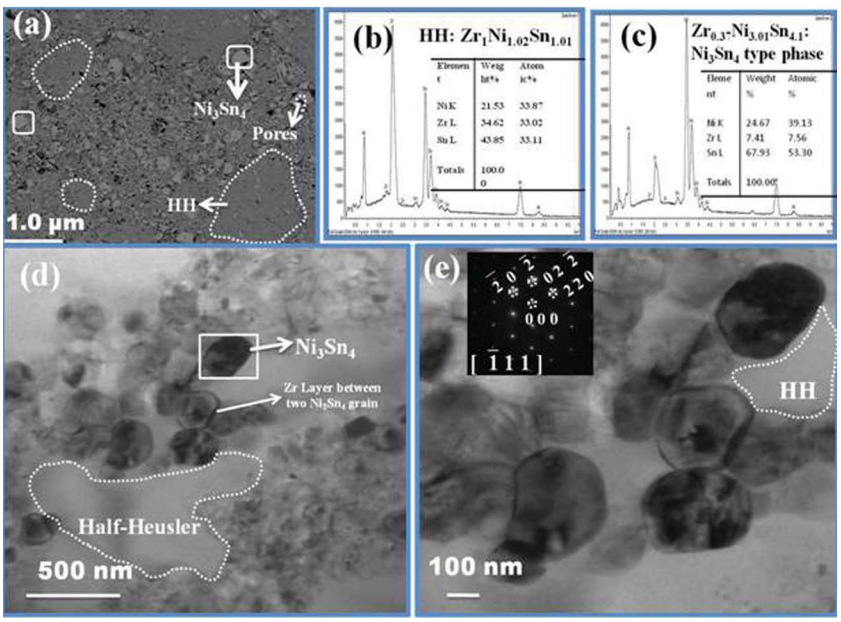

Fig. 2 (a) SEM morphology of BC $Zr_9Ni_7Sn_8$ showing a composite consisting of two phases of HH (dotted circles), Ni_3Sn_4 (square boxes) and small pores. (b) EDAX-SEM recorded from a dotted portion in (a), shows the presence of all the elements and quantification shows a phase very close to the HH. (c) EDAX-SEM obtained from a region marked as a square box in (a) shows the presence of Ni, Sn & Zr elements and quantification shows a phase very close to the Ni_3Sn_4-type phase with Zr surrounding the grain boundaries of Ni_3Sn_4 phase. (d) Bright field TEM image also shows two contrasts in the sample which confirm the presence of two phases. (e) High magnification TEM image clearly shows two phases. The inset, shows the SAED pattern corresponding to the dotted region, revealing the HH phase with zone axis [1 $\bar{1}$ 1].

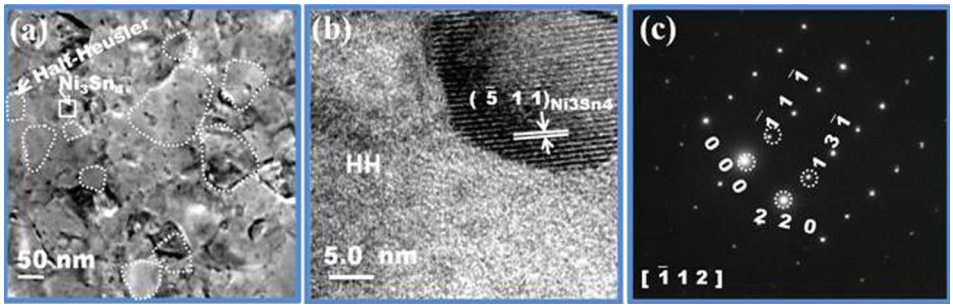

Fig. 3 (a) TEM image of $Zr_9Ni_7Sn_8$-BNC showing varying grain sizes of 45 to 170 nm of HH indicated by dotted lines and varying sizes of 5 to 25 nm of Ni_3Sn_4 shown by square boxes. (b) HRTEM image shows the two phases; HH and Ni_3Sn_4 with (−5, 1, 1) lattice planes. (c) SAED pattern corresponding to a dotted region, showing the HH phase with zone axis [1 $\bar{1}$ 2].

room temperature σ of the BC sample of $Zr_9Ni_7Sn_8$ is observed to be significantly higher in comparison to that of HH. However, the BNC sample exhibits two striking features *i.e.* reduction in σ compared to the BC sample but higher than the normal HH counterpart and a weak temperature dependency of $\sigma(T)$. For instance, room temperature values of σ of HH, BC, and BNC are

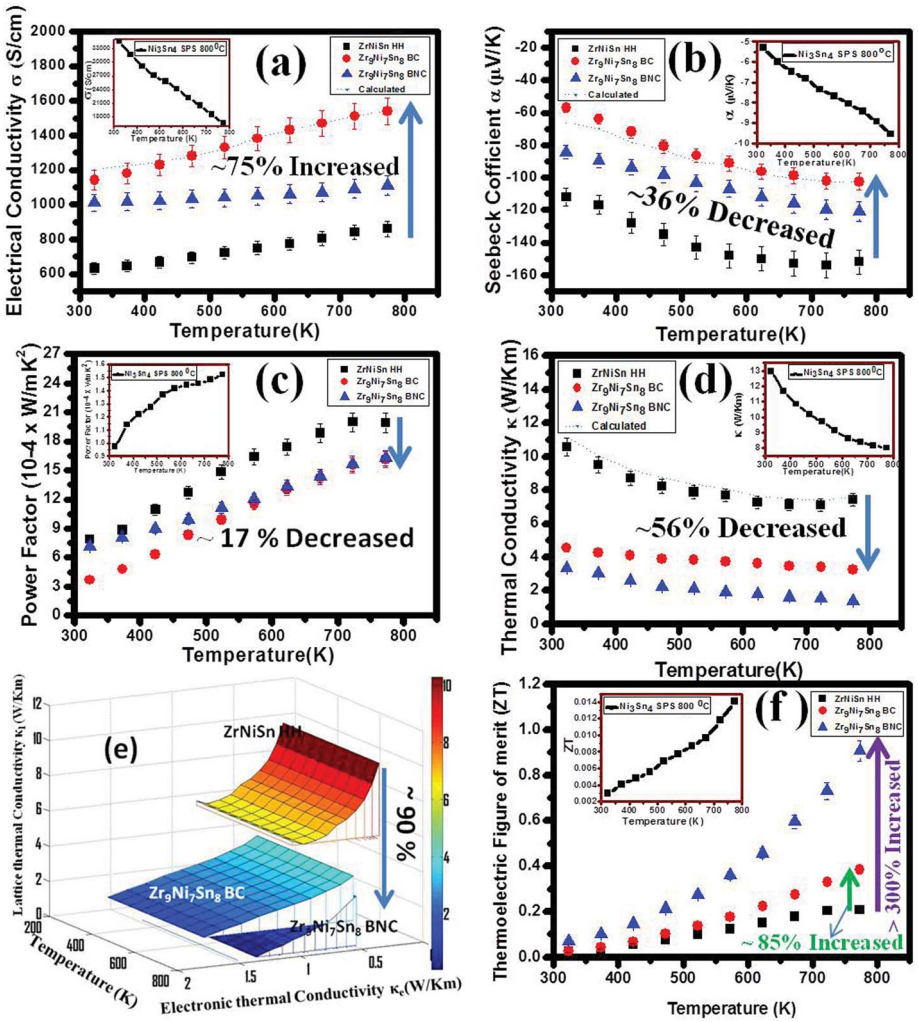

Fig. 4 Temperature dependence of thermoelectric properties of ZrNiSn normal HH, $Zr_9Ni_7Sn_8$ bulk composite (BC), $Zr_9Ni_7Sn_8$ bulk nanocomposite (BNC) and Ni_3Sn_4 [inset] and calculated effective thermoelectric parameters for the composites using the Bergemen and Fel model: (a) electrical conductivity, (b) Seebeck coefficient, (c) power factor, (d) total thermal conductivity, (e) lattice and electronic thermal conductivity and (f) calculated thermoelectric figure of merit (*ZT*).

632 S cm^{-1}, 1140 S cm^{-1} and 1010 S cm^{-1}, respectively. This corresponds to an increase in σ of ~80% for BC and ~60% for BNC, compared to normal HH ZrNiSn. The increased σ of BC and BNC samples might result from the large carrier density induced by doping of the HH matrix by the metallic Ni_3Sn_4-type phase. Fig. 4b shows the temperature dependence of the Seebeck coefficient (α) of HH, BC, BNC which indicates they are n-type materials. The value of room temperature α of BC and BNC samples is significantly lowered compared to the bulk HH counterpart and this decrease is associated with the increase in the corresponding σ. For instance, the room temperature values of α in HH, BC and BNC are −122, −56.8, and −84.3 μV K^{-1}, respectively, which corresponds to ~115% and ~45% decrease compared to the value of the HH counterpart.

In order to understand the behavior of electronic transport, room temperature Hall-effect measurements have been performed on HH, BC, and BNC samples to measure the carrier density. The carrier mobility was calculated from the electrical conductivity value. The BC sample exhibited a carrier concentration of 1.6×10^{20} cm^{-3} and mobility of ~42 cm^2 V^{-1} s^{-1} while the BNC sample yielded a carrier concentration of 9.3×10^{19} cm^{-3} and mobility ~72 cm^2 V^{-1} s^{-1}. The carrier concentration and mobility for the HH sample were found to be 2.4×10^{19} cm^{-3} and ~167 cm^2 V^{-1} s^{-1}, respectively. The large increase in σ of BC is attributed to the increased carrier density arising from doping of HH with Ni_3Sn_4 precipitates. The observed decrease in α of BC and BNC samples compared to the bulk counterpart matrix of HH is consistent with the increased carrier densities in comparison to the HH counterpart. Remarkably, the increase in α for the BNC sample compared to that of the BC sample could be attributed to the observed reduction in carrier density at around 300 K which might have resulted due to filtering of the low energy carriers by scattering at the potential barrier created at the interfaces of HH/Ni_3Sn_4, similar to that proposed by Faleev *et al.*,[50] in the BNC sample. Such a filtering effect will not occur in the BC sample due to the submicron size of the Ni_3Sn_4 phase. Only the optimum size of inclusions ranging from 2–20 nm promotes such a filtering effect, as suggested by Faleev *et al.*[50]

A plausible explanation for the mechanism of the increased α of the BNC compared to its bulk counterpart BC sample may also be discussed in the frame of a model involving the scattering factor and reduced Fermi energy proposed by Nolas *et al.*[51] where α is expressed as:

$$\alpha = \frac{\pi^2}{3}\frac{K_B}{e}\left(r+\frac{2}{3}\right)\left(\frac{1}{\xi}\right)$$

where K_B is the Boltzmann constant, r is the scattering factor and ξ is the reduced Fermi energy. A significant decrease in the carrier concentration in nanocomposite (BNC) $Zr_9Ni_7Sn_8$ as seen from the Hall data, may reduce the Fermi energy and consequently result in an increased α as compared to its BC sample. Additionally, the increase in α of the BNC sample may also be attributed to an increased scattering factor r, apparently from the potential barrier scattering effect.[52] It is worth mentioning here that similar effects have also been reported in HH ZrNiSn/ZrO_2 based nanocomposites.[52] Nevertheless, further studies may be required to understand the mechanism leading to the increase in the scattering factor and the electron filtering effects. Thus, it appears that the overall effect of metallic Ni_3Sn_4 inclusions on the electronic transport of the nanocomposite might be related to several factors, such as optimum size, carrier concentration, potential profile in the bulk matrix and the position of the Fermi level compared to its bulk counterpart. The temperature dependence of the power factor, plotted in Fig. 4c, is found to decrease in both BC and BNC samples as compared to the HH counterpart. This decrease in power factor in both samples is attributed to the drastic reduction in α due to metallic Ni_3Sn_4 doping in HH, as compared to the value in the HH counterpart.

In addition to α and σ, the thermal conductivity, κ is also an important parameter for a thermoelectric material. The thermal conductivity is calculated by taking the product of diffusivity, specific heat and density of the sample. These data for the samples are shown in the ESI as Fig. S1, S2 & Table T1,†respectively. The value of κ of sample BC is significantly reduced by −56% in comparison to the HH, as shown in Fig. 4d. This drastic reduction in κ of the BC sample may be partly attributed to the lattice expansion of HH which leads to lattice softening resulting from weak chemical bonding, resulting in dampening of the phonon propagation in addition to the interface scattering of phonons from phase boundaries. This observation is similar to our earlier report.[46] Interestingly, the κ of the BNC sample is significantly reduced by ~81%, as evident from Fig. 4d, in comparison to that of the normal HH counterpart. The significantly reduced κ of the BNC sample may be assigned to a high density of HH/Ni_3Sn_4 hetero-interfaces in addition to notable mesoscale grain boundaries for enhanced scattering of phonons ranging from large-to-medium-to-short wavelengths.

In order to understand the details of the effect of interfaces on the κ_l of the BC and BNC samples, the lattice thermal conductivity (κ_l) was calculated by subtracting the electronic part of thermal conductivity (κ_e) from the total thermal conductivity (κ),[54] using the Wiedemann–Franz law. The Wiedemann–Franz law is invoked to calculate the electronic part of the thermal conductivity, by the relationship $\kappa_e = L_0\sigma T$, where L_0 is the Lorenz number,[55] $L_0 = 2.48 \times 10^{-8}$ W Ω K^{-2}, for a metallic-like material and the bipolar contribution was taken into account by assuming $\kappa_l \approx 1/T$.[53] Fig. 4e suggests that for the HH sample, $\kappa_e = 0.31$ W m^{-1} K^{-1} and $\kappa_l = 10.57$ W m^{-1} K^{-1} (at room temperature) whereas, for the BC and BNC samples, the κ_e vales were found to be 0.52 W m^{-1} K^{-1} and 0.49 W m^{-1} K^{-1}, respectively, and κ_l; 4.03 W m^{-1} K^{-1} and 2.86 W m^{-1} K^{-1}, respectively. Thus it can be easily inferred from Fig. 4e that κ_l dominates over κ_e and the HH sample has a significantly higher κ_l value. It was noted that a 60% and 72% decrease in κ_l is observed for the BC and BNC samples, respectively, in comparison to the value of HH. This significant reduction in lattice thermal conductivity κ_l primarily contributes to a large enhancement in ZT for BC and BNC samples. For instance, the BC sample exhibits a ZT of ~0.38 at 773 K and the BNC sample has a ZT of approximately 0.90 at 773 K, which are ~85% and >300% higher than that of the HH. The variation in ZT as a

function of temperature is shown in Fig. 4f. The stability of the material and consistency of electronic transport properties have been verified by measuring the electrical conductivity and Seebeck coefficient of samples after being kept at room temperature for 10 weeks and also with the samples annealed at 850 °C for 24 h, which are presented in the ESI (Fig. S3 & S4†, respectively). We do not find a significant change in the values of electrical conductivity and Seebeck coefficient (Fig. S3 & S4†) in the composites. The temperature dependent α, σ and κ of both BC and BNC were observed to be consistent in magnitude and also in trends of α and σ suggesting these materials to be chemically stable in nature.

3.3 Bergman–Fel effective medium model: calculation of effective thermoelectric parameters

In order to discuss our observed results, the Bergman–Fel effective medium model[40,41] has been used to calculate the effective value of thermoelectric parameters. This model relates the effective electrical conductivity $\sigma_{(E)}$, effective thermal conductivity $\kappa_{(E)}$ and effective Seebeck coefficient $\alpha_{(E)}$ for a composite containing a random dispersion of nearly spherical particle inclusions in a matrix medium. If one assumes a matrix medium such as HH as A and inclusion of Ni_3Sn_4 as B in the present study, and σ_A and σ_B the electrical conductivities, α_A and α_B the Seebeck coefficients, κ_A and κ_B as the thermal conductivities of the constituents A & B respectively, then the effective σ_E, κ_E and α_E for such a composite can be given as:

$$\sigma_E = \sigma_A + \frac{\phi}{D}\left(\frac{\delta_\sigma}{d_{BA}} + \frac{1-\phi}{3}\frac{\sigma_A}{d_A}\right) \quad (1)$$

$$\kappa_E = \kappa_A + \left(\frac{\delta_\kappa}{d_{BA}} + \frac{1-\phi}{3}\frac{\kappa_A}{d_A}\right) \quad (2)$$

$$\alpha_E = \left[\alpha_A\sigma_A + \frac{\phi}{D}\left(\frac{\phi_{\alpha\sigma}}{d_{BA}} + \frac{1-\phi}{3}\frac{\alpha_A\sigma_A}{d_A}\right)\right]\frac{1}{\sigma_E} \quad (3)$$

where ϕ is the volume fraction of phase B and $\delta_\sigma \equiv \sigma_B - \sigma_A$, $\delta_\kappa \equiv \kappa_B - \kappa_A$,

$$d_A \equiv \frac{\sigma_A\kappa_\partial}{T} - (\alpha_A\sigma_A)^2,\ d_{BA} \equiv \frac{\delta_\sigma\delta_\kappa}{T} - {\delta_{\alpha\sigma}}^2$$

and

$$D \equiv \left(\frac{\delta_\sigma}{d_{BA}} + \frac{1-\phi}{3}\frac{\sigma_A}{d_A}\right)\left(\frac{\delta_\kappa}{Td_{BA}} + \frac{1-\phi}{3}\frac{\kappa_A}{Td_A}\right) - \left(\frac{\delta_{\alpha\sigma}}{d_{BA}} + \frac{1-\phi}{3}\frac{\alpha_A\sigma_A}{d_A}\right)^2$$

The calculation of effective TE parameters for a composite was performed considering a 25% volume fraction of Ni_3Sn_4 inclusions in the HH matrix, as obtained by Reitveld refinement. Accordingly, the $\sigma_{(E)}$, $\alpha_{(E)}$ and $\kappa_{(E)}$ of bulk HH/Ni_3Sn_4 composite are calculated using eqn (1)–(3) and are plotted in Fig. 4a, b & d, respectively. The σ, α and κ of Ni_3Sn_4 phase are shown in the insets of Fig. 4a, b & d, respectively. It can be clearly noted from Fig. 4a and b that the calculated data for σ_E and α_E present a slightly deviated trend with small variations in their magnitude as compared to the observed experimental results for the BC sample. This slight deviation in σ_E and α_E is expected and can be attributed to the presence of a trace amount of a third phase of Zr at the grain boundary of Ni_3Sn_4 as evidenced by SEM-EDAX analysis (Fig. 2c). However, when compared to the calculated data for the BNC sample, neither σ_E nor α_E matches with the experimental results for BNC sample which is quite expected as model assumes a micron-sized inclusion phase rather than a nano-sized inclusion in the matrix phase. It is interesting to mention here that the Hall data and transport properties, discussed in Section 3.2, also revealed the filtering effect and interface boundary scattering in our BNC sample, which supports the devaition of the assumptions of the Bergmann–Fell model, and hence an inconsistency in the calculated and observed thermoelectric parameters was observed.

The size and distribution of Ni_3Sn_4 nano-inclusions in the composite influences the transport properties of the BNC sample. It is important to mention that the BNC sample exhibited a rather high α (in Fig. 4b) without changing the carrier concentration in comparison to its BC counterpart. The exact reason for this result is not yet clearly known. However, it could be an energy filtering mechanism, similar to that proposed by Faleev *et al.*,[50] as discussed in Section 3.2. In the present work, low energy carriers might have been filtered out by the scattering at the potential barrier created at the interface between HH and metallic Ni_3Sn_4 phases and thus improvement in α of the BNC sample in comparison to its BC counterpart, as discussed previously. Thus, the optimum size and density of the Ni_3Sn_4 precipitates could be an important factor responsible for enhancing the *ZT*.

The results obtained in the present work motivate the design of the *in situ* bulk composite consisting of HH and metallic inclusions of Ni_3Sn_4 in a non-stiochiometric HH composite with a VEC smaller than 18 for a drastic reduction in κ and simultaneous improvement in the electrical transport. However, further work is needed to explore several compositions of half-Heuslers of the XYZ family to assess the precise impact of such composite materials on the thermoelectric properties. Moreover, optimization of several processing conditions and their impact on thermoelectric properties in $Zr_9Ni_7Sn_8$ may be a future avenue of the present research.

4. Conclusions

An non-stoichiometric composition of a HH, namely $Zr_9Ni_7Sn_8$, having a VEC of 17.5 per unit formula which is smaller than 18 for the most stable normal ZrNiSn HH, exhibits an *in situ* composite of HH/Ni_3Sn_4 rather than forming a superstructure of HH. Such an *in situ* composite enables achievement of a high *ZT* of ~0.38 at 773 K, which is ~85% higher in comparison with that of the normal HH counterpart. Interestingly, nanostructuring of the BC sample further enhanced *ZT* to ~0.90 at 773 K, which is >300% higher than the normal HH counterpart. The enhancement in *ZT* for BC and BNC samples is primarily due to a significant reduction in their κ with simultaneous improvement in electrical conductivity, as compared to the

normal HH counterpart. Our finding stimulates the search for several non-stoichiometric compositions based on varying the VEC in the wider family of XYZ (X = Ti, Zr, Hf, Y = Ni, Co, Z = Sn, Sb) with composition $X_{1+x}Y_{1-x}Z$ where significant reduction in thermal conductivity and electronic transport can be optimized for high *ZT* values. Further controlling the distribution of metallic inclusions by fine tuning the growth parameters through appropriate thermal-treatment and with or without doping could be a promising future strategy for enhancing the *ZT* of several compositions of the HH family.

Acknowledgements

This work was financially supported by CSIR-TAPSUN (CSIR-NWP-54) programme. The authors thank Prof. R. C. Budhani and Dr Jiji Pullikotil for useful discussions and comments. We acknowledge Dr. Ajay Dhar (HOD, Metals and Alloys Group) for providing facilities and his critical comments for successful completion of the present work. One of the authors, AB, greatly acknowledges UGC-CSIR for financial support. We thank Radheshyam and Naval K. Upadhyay for technical and experimental support.

References

1 G. Chen, M. S. Dresselhaus, G. Dresselhaus, J. P. Fleurial and T. Caillat, *Int. Mater. Rev.*, 2003, **48**, 45.
2 B. Poudel, Q. Hao, Y. Ma, Y. Lan, A. Minnich, B. Yu, X. Yan, D. Wang, A. Muto, D. Vashaee, X. Chen, J. Liu, M. S. Dresselhaus, G. Chen and Z. Ren, *Science*, 2008, **320**, 634.
3 S. Yu, J. Yang, Y. Wu, Z. Han, J. Lu, Y. Xie and Y. Qian, *J. Mater. Chem.*, 1998, **8**, 1949.
4 J. Shen, T. Zhu, X. Zhao, S. Zhang, S. Yanga and Z. Yina, *Energy Environ. Sci.*, 2010, **3**, 1519.
5 M. E. Anderson, S. S. N. Bharadwaya and R. E. Schaak, *J. Mater. Chem.*, 2010, **20**, 8362.
6 S. Sumithra, N. J. Takas, D. K. Misra, W. M. Nolting, P. F. P. Poudeu and K. L. Stokes, *Adv. Energy Mater.*, 2011, **1**, 1141.
7 K. F. Hsu, S. Loo, F. Guo, W. Chen, J. S. Dyck, C. Uher, T. Hogan, E. K. Polychroniadis and M. G. Kanatzidis, *Science*, 2004, **303**, 818.
8 J. Androulakis, K. F. Hsu, R. Pcionek, H. Kong, C. Uher, J. J. D'Angelo, A. Downey, T. Hogan and M. G. Kanatzidis, *Adv. Mater.*, 2006, **18**, 1170.
9 J. R. Sootsman, H. Kong, C. Uher, J. J. D'Angelo, C. I. Wu, T. P. Hogan, T. Caillat and M. G. Kanatzidis, *Angew. Chem., Int. Ed.*, 2008, **47**, 8618.
10 R. Basu, S. Bhattacharya, R. Bhatt, M. Roy, S. Ahmad, A. Singh, M. Navaneethan, Y. Hayakawa, D. K. Aswal and S. K. Gupta, *J. Mater. Chem. A.*, 2014, **2**, 6922.
11 J. J. Pulikkotil, D. J. Singh, S. Auluck, M. Saravanan, D. K. Misra, A. Dhar and R. C. Budhani, *Phys. Rev. B: Condens. Matter Mater. Phys.*, 2012, **86**, 155204.
12 S. R. Brown, S. M. Kauzlarich, F. Gascoin and G. J. Snyder, *Chem. Mater.*, 2006, **18**, 1873.
13 G. J. Snyder, M. Christensen, E. Nishibori, T. Caillat and B. B. Iversen, *Nat. Mater.*, 2004, **3**, 458.
14 S. K. Bux, A. Zevalkink, O. Janka, D. Uhl, S. Kauzlarich, J. G. Snyder and J. P. Fleurial, *J. Mater. Chem. A*, 2014, **2**, 215.
15 A. Bhardwaj, A. Rajput, A. K. Shukla, J. J. Pulikkotil, A. K. Srivastava, A. Dhar, G. Gupta, S. Auluck, D. K. Misra and R. C. Budhani, *RSC Adv.*, 2013, **3**, 8504.
16 S. R. Culp, S. J. Poon, N. Hickman, T. M. Tritt and J. Blumm, *Appl. Phys. Lett.*, 2006, **88**, 042106.
17 R. A. Downie, D. A. MacLaren and J.-W. G. Bos, *J. Mater. Chem. A*, 2014, **2**, 6107.
18 R. A. Downie, D. A. MacLaren, R. I. Smith and J.-W. G. Bos, *Chem. Commun.*, 2013, **49**, 4184.
19 C. Uher, J. Yang, S. Hu, D. T. Morelli and G. P. Meisner, *Phys. Rev. B: Condens. Matter Mater. Phys.*, 1999, **59**, 8615.
20 J. Kübler, A. R. Williams and C. B. Sommers, *Phys. Rev. B: Condens. Matter Mater. Phys.*, 1983, **28**, 1745.
21 C. Felser, G. H. Fecher and B. Balke, *Angew. Chem., Int. Ed.*, 2007, **46**, 668.
22 S. Chadov, X. Qi, J. Kübler, G. H. Fecher, C. Felser and S. C. Zhang, *Nat. Mater.*, 2010, **9**, 541.
23 H. Lin, A. Wray, Y. Xia, S. Xu, S. Jia, R. J. Cava, A. Bansil and M. Z. Hasan, *Nat. Mater.*, 2010, **9**, 546.
24 I. Takeuchi, O. O. Famodu, J. C. Read, M. A. Aronova, K.-S. Chang, C. Craciunescu, S. E. Lofland, M. Wuttig, F. C. Wellstood, L. Knauss and A. Orozco, *Nat. Mater.*, 2003, **2**, 180.
25 P. Entel, V. D. Buchelnikov, V. V. Khovailo, A. T. Zayak, W. A. Adeagbo, M. E. Gruner, H. C. Herper and E. F. Wassermann, *J. Phys. D: Appl. Phys.*, 2006, **39**, 865.
26 D. B. Xiong, Y. Zhao, N. L. Okamoto, C. Pietzonka, T. Waki and H. Inui, *Inorg. Chem.*, 2010, **49**, 10536.
27 W. Kim, J. Zide, A. Gossard, D. Klenov, S. Stemmer, A. Shakouri and A. Majumdar, *Phys. Rev. Lett.*, 2006, **96**, 045901.
28 M. S. Dresselhaus, G. Chen, M. Y. Tang, R. G. Yang, H. Lee, D. Z. Wang, Z. F. Ren, J. P. Fleurial and P. Gogna, *Adv. Mater.*, 2007, **19**, 1043.
29 J. W. Sharp, S. J. Poon and H. J. Goldsmid, *Phys. Status Solidi A*, 2001, **187**, 507.
30 S. Bhattacharya, T. M. Tritt, Y. Xia, V. Ponnambalam, S. J. Poon and N. Thadhani, *Appl. Phys. Lett.*, 2002, **81**, 43.
31 J. M. Zide, D. Vashaee, Z. X. Brian, G. Zeng, J. E. Bowers, A. Shakouri and A. C. Gossard, *Phys. Rev. B: Condens. Matter Mater. Phys.*, 2006, **74**, 205335.
32 M. Zebarjadi, K. Esfarjani, A. Shakouri, Z. X. Bian, J. H. Bahk, G. Zeng, J. E. Bowers, H. Lu, J. M. O. Zide and A. Gossard, *J. Electron. Mater.*, 2009, **38**, 954.
33 J. P. Heremans, *Acta Phys. Pol., A*, 2005, **4**, 609.
34 H. Ohta, S. W. Kim, Y. Mune, T. Mizoguchi, K. Nomura, S. Ohta, T. Nomura, Y. Nakanishi, Y. Ikuhara, M. Hirano, H. Hosono and K. Koumoto, *Nat. Mater.*, 2007, **6**, 129.
35 R. S. Makala, K. Jagannadham and B. C. Sales, *J. Appl. Phys.*, 2003, **94**, 3907.
36 A. I. Hochbaum, R. Chen, R. D. Delgado, W. Liang, E. C. Garnett, M. Najarian, A. Majumda and P. Yang, *Nature*, 2008, **451**, 163.

37 A. I. Boukaiet, Y. Bunimovich, J. T. Kheli, J. K. Yu, W. A. Goddard and J. R. Heath, *Nature*, 2007, **451**, 168.
38 J. L. Mi, X. B. Zhao, T. J. Zhu and J. P. Tu, *Appl. Phys. Lett.*, 2007, **91**, 172116.
39 L. D. Zhao, B. P. Zhang, W. S. Liu and J. F. Li, *J. Appl. Phys.*, 2009, **105**, 023704.
40 D. J. Bergman and O. J. Levy, *J. Appl. Phys.*, 1991, **70**, 6821.
41 D. J. Bergman and L. G. Fel, *J. Appl. Phys.*, 1999, **85**, 8205.
42 J. P. Heremans and C. M. Jaworski, *Appl. Phys. Lett.*, 2008, **93**, 122107.
43 T. He, J. Chen, H. D. Rosenfeld and M. A. Subramanian, *Chem. Mater.*, 2006, **18**, 759.
44 W. S. Liu, B. P. Zhang, L. D. Zhao and J. F. Li, *Chem. Mater.*, 2008, **20**, 7526.
45 H. Li, X. F. Tang, Q. J. Zhang and C. Uher, *Appl. Phys. Lett.*, 2009, **94**, 102114.
46 A. Bhardwaj, D. K. Misra, J. J. Pulikkotil, S. Auluck, A. Dhar and R. C. Budhani, *Appl. Phys. Lett.*, 2012, **101**, 133103.
47 J. P. A. Makongo, D. K. Misra, X. Zhou, A. Pant, M. R. Shabetai, X. Su, C. Uher, K. L. Stokes and P. F. P. Poudeu, *J. Am. Chem. Soc.*, 2011, **133**, 18843.
48 J. P. A. Makongo, D. K. Misra, J. R. Salvador, N. J. Takas, G. Wang, M. R. Shabetai, A. Pant, P. Paudel, C. Uher, K. L. Stokes and P. F. P. Poudeu, *J. Solid State Chem.*, 2011, **184**, 2948.
49 X. Yan, G. Joshi, W. S. Liu, Y. C. Lan, H. Wang, S. Lee, J. W. Simonson, S. J. Poon, T. M. Tritt, G. Chen and Z. F. Ren, *Nano Lett.*, 2011, **11**, 556.
50 S. V. Faleev and F. Léonard, *Phys. Rev. B: Condens. Matter Mater. Phys.*, 2008, **77**, 214304.
51 G. S. Nolas, J. Sharp and H. J. Goldsmid, *Thermoelectrics: Basic Principles and New Materials Developments*, Springer, Berlin, 2001.
52 L. I. Bytenskii, T. S. Gudkin, E. K. Iordanishvili, S. A. Kazmin, V. I. Kaidanov and S. A. Nemov, *Soviet Physics – Semiconductors*, 1977, **11**, 894.
53 L. D. Chen, X. Y. Huang, M. Zhou, X. Shi and W. B. Zhang, *J. Appl. Phys.*, 2006, **99**, 064305.
54 H. Kitagawa, M. Wakatsuki, H. Nagaoka, H. Noguchi, Y. Isoda, K. Hasezaki and Y. J. Noda, *J. Phys. Chem. Solids*, 2005, **66**, 1635.
55 W. S. Liu, B. P. Zhang, J. F. Li, H. L. Zhang and L. D. Zhao, *J. Appl. Phys.*, 2007, **102**, 103717.